Attenuated total reflection infrared spectroscopy for studying adsorbates on planar model catalysts : CO adsorption on silica supported Rh nanoparticles

Attenuated total reflection infrared spectroscopy for studying adsorbates on planar model catalysts: CO adsorption on silica supported Rh nanoparticles

C. M. Leewis
Department of Chemical Engineering and Department of Applied Physics, Eindhoven University of Technology, P.O. Box 513, 5600 MB Eindhoven, The Netherlands

W. M. M. Kessels and M. C. M. van de Sanden[a)]
Department of Applied Physics, Eindhoven University of Technology, P.O. Box 513, 5600 MB Eindhoven, The Netherlands

J. W. Niemantsverdriet
Department of Chemical Engineering, Eindhoven University of Technology, P.O. Box 513, 5600 MB Eindhoven, The Netherlands

(Received 8 September 2005; accepted 9 January 2006; published 17 February 2006)

A sensitive method is presented for studying adsorption of gaseous species on metal surfaces in vacuum by attenuated total internal reflection Fourier transform infrared spectroscopy (ATR). The method is illustrated by CO adsorption experiments on silica supported Rh nanoparticles. An experimental setup and a procedure are described in detail to obtain a sensitivity of reflectance change of $\sim 5 \times 10^{-5}$ absorbance units. Here, a silicon ATR crystal with a 50 nm layer of hydroxylated silica acts as the support for the Rh nanoparticles. These particles are easily prepared by spincoat impregnation from a $RhCl_3$ solution followed by H_2 reduction. X-ray photoelectron spectroscopy before and after reduction shows that rhodium is reduced to Rh^0 and that all chlorine is removed. Atomic force microscope images the distribution of the particles, which are 3–4 nm in height. When the crystal is exposed to pressures up to 1 mbar of CO, a gas which is inert to the silica support, the stretch vibration of linearly adsorbed CO on the Rh nanoparticles is detected at 2023 cm^{-1}, while no bridged CO or geminal dicarbonyl species can be distinguished. The minimum detectable coverage is estimated ~ 0.005 CO per nm^2 substrate area or $\sim 5 \times 10^{-4}$ ML. © *2006 American Vacuum Society.* [DOI: 10.1116/1.2171707]

I. INTRODUCTION

Systems consisting of metallic nanoparticles on a planar support are commonly used as surface science models for supported catalysts.[1–4] Such models offer excellent opportunities for extensive characterization by surface sensitive techniques,[1] for morphological studies by scanning probe techniques,[2–4] and for kinetic and mechanistic investigations.[5] However, possibilities for studying adsorbed species, e.g., by vibrational techniques, are limited. Successful approaches have been taken by Goodman and co-workers[6] using reflection absorption infrared spectroscopy (RAIRS) on systems with a thin oxide film on a metal substrate, and by Unterhalt *et al.*,[7] who used sum-frequency generation. In this article we describe and demonstrate a setup for attenuated total reflection infrared spectroscopy (ATR-IR) by applying a silicon ATR crystal as the substrate for a thin silica film on which metal particles are applied.

The advantage of ATR-Fourier transform infrared (FTIR) is that the sensitivity is enhanced because the absorbance is proportional to the number of reflections in the ATR crystal. Many applications are found in the literature for surface science studies[8,9] and liquid phase surface adsorption studies.[10–15] Other applications are found for studies on, e.g., thin (nano)crystalline and amorphous silicon films and surfaces.[16–18] Moreover, gas phase adsorption of precursors on a very thin metallic layer of TiCN on a Si ATR crystal, in combination with hydrogen diffusion through this layer, has been studied.[19] ATR-FTIR can be quantified easily for a monolayer[8] or for an adsorbed layer that is much thinner than the penetration depth of the evanescent wave.[20] In this work, ATR-FTIR is explored to study adsorption from the gas phase on a planar model catalyst, i.e., metallic nanoparticles supported by a silica film on a Si ATR crystal.

Silicon ATR crystals have the advantage that these are easily thermally oxidized to obtain the desired silica support for the planar model catalyst. This support should preferably be thin to reduce any additional infrared attenuation in the silica but must be thick enough to avoid interaction of the metal particles with the silicon. In addition, silicon crystals are relatively cheap, considering the fact that the deposition of nanoparticles on the crystal does not allow the reuse of the crystal. However, a disadvantage of silicon is that the infrared transmittance is heavily reduced for wave numbers lower than 1500 cm^{-1}. In this work, silicon ATR crystals with a 50 nm layer of silica are considered, with bevels at an angle of 45°. Since the crystal is at room temperature, the useable spectral range is 5000–1500 cm^{-1}. For increasing temperature, the transmittance decreases and changes in the transmit-

[a)]Author to whom correspondence should be addressed; electronic mail: m.c.m.v.d.sanden@tue.nl

tance occur in the ~3500 cm^{-1} region due to OH bonds. On these crystals, Rh nanoparticles are deposited, which are easily prepared by spincoat impregnation from a solution of $RhCl_3$ in water or ethanol.[21] The effects of the silica layer and the nanoparticles on the detection of adsorbed species by the evanescent wave are discussed below.

Considering the thin silica layer on the ATR crystal, it is noted that the infrared light is internally reflected at the interface between the silicon and the silica. Since the refractive index of vacuum is also lower than that of silicon, and because the silica layer is much thinner than the penetration depth d_p, the evanescent wave extends into the vacuum. For wave numbers around 2000 cm^{-1} and an angle of incidence of 45°, the penetration depth of the evanescent wave is about 0.4 μm.[20,22,23] For 50 nm of silica, this results in a decrease in the absorbance for the adsorbed species to ~80% of the absorbance without silica layer. Therefore, the thin silica layer has little influence on the sensitivity of the current ATR experiment.

The metallic particles can heavily affect the total transmittance and adsorbate detection sensitivity. Because of the high imaginary part of the refractive index for metallic particles or films, the light can be heavily attenuated. As a reference, for a crystal fully covered with a 4 nm film of Rh, light is attenuated to ~0.3 of its initial intensity for every reflection, and there is virtually no transmittance in our case of 25 reflections, as will be discussed later. This effect is reduced for a less than fully covered crystal, where the attenuation only occurs on metal covered areas. In addition, for metallic nanoparticles, enhancement of the electric field can occur on the surface, resulting in an enhancement of the infrared adsorption.[24,25] However, for multiple reflections, densely distributed particles can easily lead to a too high infrared attenuation. Therefore, one should be able to tune both the particle size and the distribution carefully in order to reduce the effect of attenuation, and still benefit from the multiple reflections. As a side note, for a thick layer on top of the ATR crystal, frustrated internal reflection would occur, if the real part of the refractive index is higher than that of silicon. However, for a thin layer, the infrared light is still internally reflected at the vacuum interface, resulting in an evanescent wave extending into the vacuum.

As a proof of principle of the application of ATR-FTIR to the system discussed above, we have chosen to detect CO adsorption on these silica supported Rh nanoparticles. This gas is known for its high infrared absorption cross section, and does not adsorb, react, or decompose on silica, opposed to, e.g., ethylene or ammonia, although interaction of OH groups of the support can influence the adsorption of CO on metal clusters.[26] Both CO adsorption[26–29] and coadsorption with, e.g., NH_3,[30] have been studied for supported Rh.

II. EXPERIMENT

A. Sample preparation

Trapezoidal silicon ATR crystals with dimensions of 20 $\times 50 \times 1$ mm^3 with bevels at an angle of 45° (Harrick Scientific Products, Inc.) were used for the experiments. This configuration results in 25 reflections of the infrared light on the topside. A schematic representation of the crystal is given in Fig. 1. The top of the long edge had a 50 nm thermal oxide layer, as specified by the supplier. As mentioned, the silica is required for the preparation of the nanoparticles, to avoid diffusion into or reaction with the silicon and to aid particle adhesion.

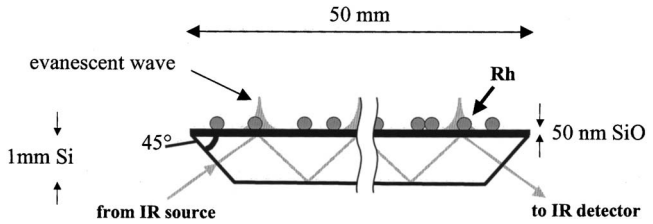

FIG. 1. Schematic representation of the silicon ATR crystal with a 50 nm silica layer that supports the Rh nanoparticles. The infrared light undergoes 25 reflections on the top interface.

The crystal was left in a "piranha" solution,[31] i.e., a 3:1 solution of H_2SO_4 and H_2O_2 at 90 °C for 1 h to remove any organic contaminants and to hydroxylate the silica, such that a hydrophilic surface is obtained. Any thin oxide layer on the bevels and backside resulting from this treatment is much thinner than the silica layer. Then, the ATR crystal was spin coated with a 1 mMol/l solution of $RhCl_3 \cdot xH_2O$ (Alfa/Johnson Matthey) in water under N_2 atmosphere at a rotation speed of 5000 rpm,[21] which resulted in dispersed nanoparticles. The $RhCl_3$ particles were then reduced to Rh^0 in a tube reactor under flowing H_2 at a pressure of 1 bar. The temperature was ramped up from room temperature to 200 °C at a rate of 3 °C/min and kept constant at 200 °C for 2 h. Afterwards, the sample was cooled down at a rate of 3 °C/min. Separate silica/silicon substrates treated in a way similar to the ATR crystal were characterized by x-ray photoelectron spectroscopy (XPS) to verify whether the reduction was successful, whereas atomic force microscope (AFM) was used to determine the average particle size and distribution. The ATR crystal was then transferred in air and mounted in the vacuum chamber.

In the vacuum setup, the alignment of the infrared beam through the ATR crystal was verified by measuring the total transmittance, after which the chamber was backed out. The Rh nanoparticles underwent another reduction step to remove any possible oxides, caused by the sample transfer. This process was similar to the one described above, except for using a H_2 pressure of about 50 mbar, followed by evacuation. The temperature was ramped to the same temperature and at the same rate as described above. After this reduction step, the Rh nanoparticles were ready for the CO exposure experiments.

XPS was applied on the silica/silicon substrate to determine the surface coverage of $RhCl_3$ and to ascertain that Cl was removed and that all Rh^{III} had been reduced to Rh^0. A VG Escalab 200 XPS system with an Al anode (Al K_α = 1486.3 eV) was used. The base pressure was 2×10^{-9} mbar, the pass energy 20 eV, the step size 0.1 eV,

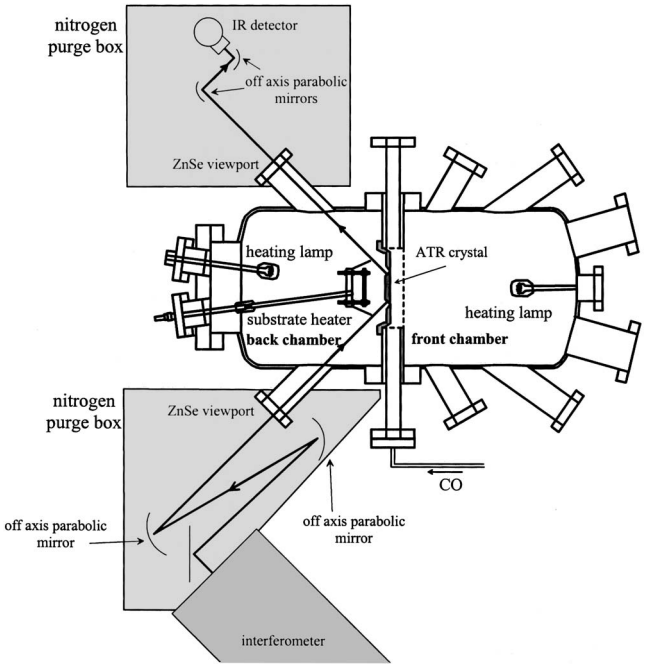

FIG. 2. Vacuum setup consisting of two individually pumped chambers, separated by a substrate holder that contains the ATR crystal. CO is admitted into the front chamber. The ATR crystal can be heated from the backside. The bevels and back side of the crystal are not exposed to gas inserted in the front chamber. The infrared beam is focused on the crystal and on the detector by two sets of focusing mirrors. The total external beam path is covered by two nitrogen purge boxes.

and the dwell time 0.1 s. The angle between the surface normal and the x-ray beam was 0°. For the regions around the Rh and Cl binding energies, 25 and 10 scans were used, respectively. The energy was calibrated with the Si $2p$ peak at a binding energy (BE) of 103.3 eV for SiO_2.[32]

AFM was applied to study the size and the distribution of the Rh nanoparticles before and after reduction on silica/silicon substrates. A vibration-stabilized NT-MDT Solver P47 AFM was used in noncontact mode with a resonant frequency of about 200 kHz with c-Si cantilevers with a tip curvature radius of 10 nm. For every sample, several images were made with scan sizes of about 2 μm $\times$ 2 μm and a lateral resolution of 2 nm.

B. Vacuum and ATR-FTIR optical setup

The high-vacuum setup, displayed in Fig. 2, consists of two chambers, individually pumped by two turbomolecular pumps, and separated by an exchangeable substrate holder,[33] in which the ATR crystal is placed. This allows gas exposure of the Rh-covered front side of the crystal only, while the bevels are optically accessed from the back side of the ATR crystal. However, upon gas dosing in the front chamber, the pressure rises in the back chamber because the ATR crystal is not perfectly leak tight. Both chambers can be baked out with an infrared heating lamp (1000 W halogen photo optic lamp) and external heating tapes. The crystal can be heated radiatively from the back side of the crystal by a substrate heater (Advanced Ceramics Corporation, Flat PBN Boralectric Heater, HTR 1002, 1440 W), which is controlled by a proportional integral differential Eurotherm 2500 temperature controller. Carbon monoxide (Praxair, purity $>99.997\%$) can be dosed in the front chamber (base pressure $\sim 10^{-9}$ mbar) by a needle valve and hydrogen (purity $>99.999\%$) by a mass flow controller. Additionally, the contaminant level for H_2 is reduced by an Aeronex Gatekeeper purifier. The pressure is set by a regulating valve between the front chamber and the turbomolecular pump. The back chamber is equipped with two ZnSe viewports (clear aperture diameter 38.6 mm) for optical access for the infrared beam. The temperature of the ATR crystal is measured by thermocouples on the substrate holder at a distance of a few mm from the crystal. A correction is applied for the temperature difference of a few K between sample and substrate holder, as deduced from reference measurements on other silicon substrates.

ATR-FTIR is used to detect the adsorption of gas species on the prepared ATR crystal. A Bruker Vector 22 infrared spectrometer with a globar light source is used, together with a liquid nitrogen cooled D313/6-M Infrared Associates infrared detector, also displayed in Fig. 2. Between the spectrometer and the entrance viewport, a set of gold mirrors, consisting of a flat mirror and two off-axis parabolic mirrors (Janostech, DP/gold coating, 45°, long focal length), focus the infrared beam on the bevel of the ATR crystal. On the side of the exit viewport, a second set of mirrors, consisting of two off-axis parabolic mirrors (90°, short focal length) focus the beam onto the detector. The infrared beam can be polarized using an external polarizer. However, for the geometry used, i.e., an internal reflection angle of 45°, the absorbance for S and P polarization have nearly the same magnitude. The polarizer is therefore omitted and nonpolarized light is used, to obtain a higher signal and sensitivity. This does not significantly influence the quantification of the absorbance in this case.[34,15] The total external beam path is covered by two purge boxes, which are flushed with pure nitrogen gas, to reduce the IR absorption by water and carbon dioxide.

Infrared spectra were taken before, during, and after CO dosing by typically averaging over 3000 scans at a resolution of 4 cm^{-1}, which takes about 10–15 min. The absorbance A was determined from a sample spectrum with transmittances I_1 and a reference spectrum before dosing with transmittance I_0, i.e., $A=-\log I_1/I_0$. For these settings, this results in a minimum detectable signal of $\sim 5\times 10^{-5}$ absorbance units in the region 4000–1500 cm^{-1}. In some cases, 2× or 3 × 3000 scans were used to reduce noise even further.

III. RESULTS

A. XPS analysis

X-ray photoelectron spectroscopy (XPS) was used to determine the state of the Rh particles before and after reduction. The spectra are shown in Fig. 3 for both Rh and Cl. The Rh $3d_{3/2}$, the Rh $3d_{3/2}$, and the Si $2p$ peak are shown. Upon reduction, the Rh $3d_{5/2}$ peak shifted from a BE of 309.4 eV

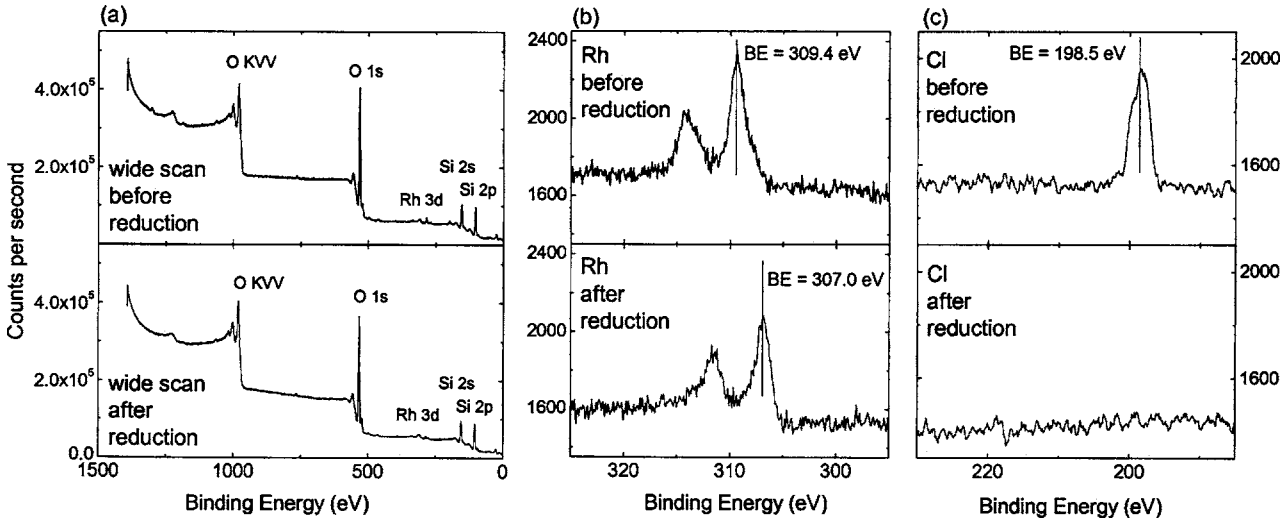

FIG. 3. XPS spectra before (top) and after (bottom) reduction calibrated with the Si $2p$ peak of SiO_2 at 103.3 eV. A widescan (a), the Rh $3d_{3/2}$ and Rh $3d_{5/2}$ peaks (b), and the Cl $2p$ peak (c) are shown, respectively. Intensities are given in counts per second.

for Rh^{III} to 307.0 eV for Rh^0. The Rh peak intensity is similar to the unreduced case. The Cl $2p$ peak at 198.5 eV BE disappeared below the detection limit of typically 0.1 at. % after reduction. Both spectra for Rh and Cl show that the reduction was successful.

B. AFM analysis

Atomic force microscopy showed particles with an average height of >5 nm before and about 3–4 nm after reduction, as shown in Fig. 4, respectively. The width of the particles, as determined with AFM, is 30–50 nm. This value is probably enlarged due to finite tip size effects. The particle density is about 200 particles/μm^2. No significant long-range nonuniformity in particle distribution due to the rectangularly shaped ATR crystal was found for the spincoat conditions used.

In Fig. 5, a histogram of the height distribution is presented for a clean silica surface, and the Rh-covered surfaces, before and after reduction. Although a distortion is expected due to the finite tip size effects, the height distributions measured for the Rh-covered samples are clearly wider than for the clean silica surface with the width of the height distribution being a measure for the particle height. After reduction, the height distribution in Fig. 5 clearly becomes narrower and the maximum and average particle heights are reduced.

C. ATR-FTIR measurements

For metallic particles or thin films, the transmission through the ATR crystal can be reduced, depending on the particle size and distribution. In a first attempt, particles with a height of 20 nm were prepared by spincoating in ethanol, which resulted in a transmittance of only ~10%–15% of that for a crystal without Rh. However, for the ATR crystals with and without the ~4 nm Rh particles in the present experiment, the values of the total transmittance had a comparable magnitude. The positioning in the setup and the infrared beam alignment for similar blank crystals can also lead to differences in transmittance, but the attenuation due to the ~4 nm Rh nanoparticles is certainly not more than 50%.

The results of the ATR-FTIR measurements on the CO exposure to the Rh-covered ATR crystal are shown in Fig. 6. The spectra shown were obtained by averaging over 3×3000 scans with a resolution of 4 cm^{-1}, using nonpolarized light to obtain a maximum signal. As a reference spectrum, a measurement with 3×3000 scans before dosing was used. A small base line correction was required for the three upper spectra in Fig. 6(a) to correct for long-term temperature fluctuations in the globar. The spectra were obtained before dosing, during dosing for increasing pressures, and after evacuation. A linearly adsorbed CO stretch peak is observed at 2023 cm^{-1} at a pressure of 2×10^{-2} mbar. The area of this peak increases with pressure. At pressures higher than 3×10^{-1} mbar, the P and R branches of gas phase CO are distinguished with a center frequency of 2143 cm^{-1}. After assumingly saturating the sample at 1 mbar, resulting in a pressure of 3.5×10^{-3} mbar in the back chamber, the front chamber was evacuated. After evacuation, only the peak of linearly adsorbed CO remained. The integrated peak area is 9×10^{-3} absorbance units $\times$ cm^{-1}, while the peak width is about 90 cm^{-1}. The lowest detectable absorbance, as estimated from Fig. 6(a), is about $\sim 3 \times 10^{-5}$ absorbance units, which corresponds to $\sim 5 \times 10^{-5}$ absorbance units for 1 $\times 3000$ scans.

The same CO exposure experiment was performed on a similarly hydroxylated silica/silicon ATR crystal without Rh particles. These results are displayed in Fig. 6(b). The noise level is slightly higher because averaging was done over only 2×3000 scans instead of 3×3000. As expected, no adsorbed CO is observed for this sample, indicating that CO on Rh is observed for the Rh-covered crystal. In addition, the magnitude of the absorption by gas phase CO is ~30% higher than for the sample with Rh.

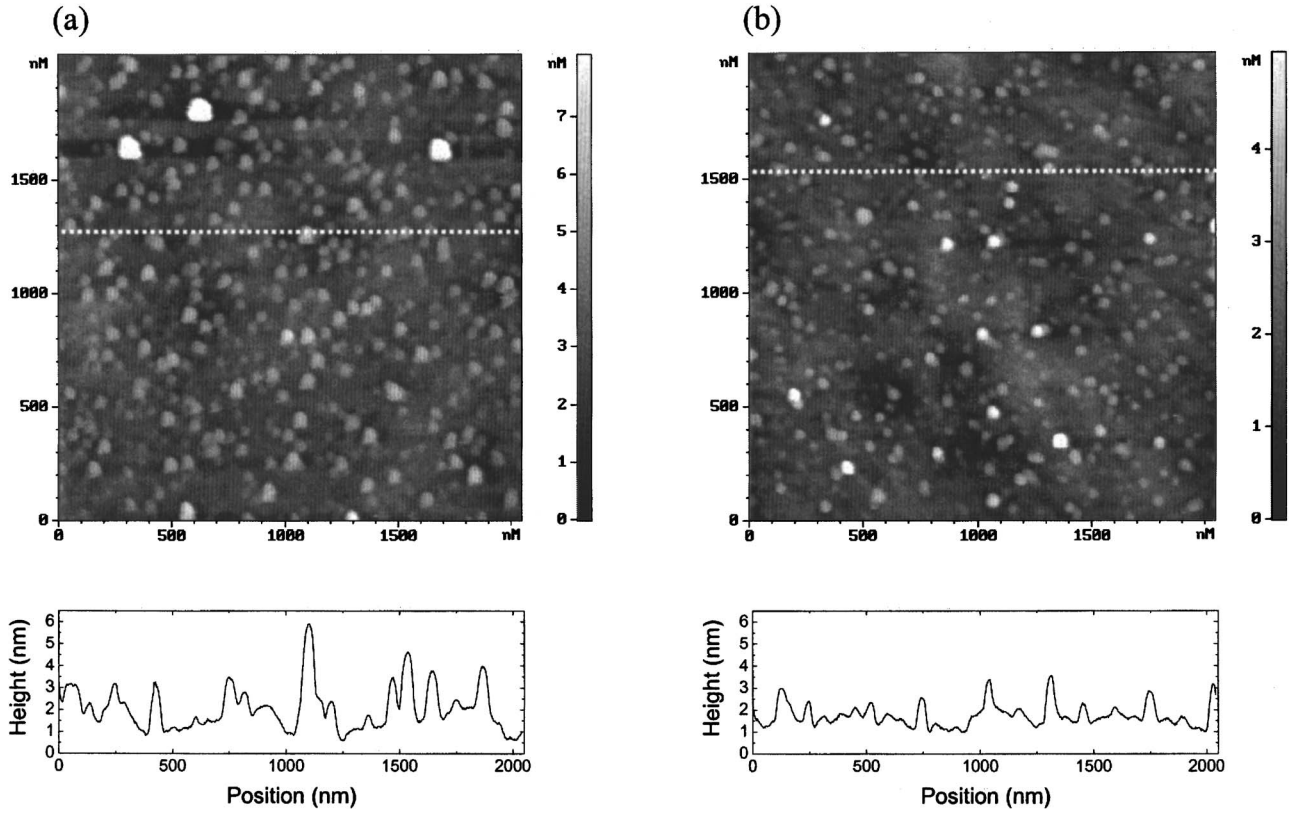

FIG. 4. AFM images and typical cross sections before (a) and after (b) reduction of the silica supported Rh nanoparticles. After reduction, the particle height is slightly reduced.

IV. DISCUSSION

As shown by the XPS experiments, the Rh and Cl binding energies for the unreduced sample correspond within 0.2 eV to values found in the literature for comparable $RhCl_3$ systems.[35,36] The Rh^0 binding energy of 307.0 eV is bulk like, suggesting that the Rh particles contain at least hundreds of atoms.[37,21] The Rh/Si ratio for this sample was found to be 0.16–0.20, which is somewhat lower than 0.24–0.35 for comparable systems with a Rh loading of ~ 5 atoms/nm^2 reported in the literature.[21]

It is shown by AFM that the particles become smaller after reduction. This is consistent with the literature[35,36] where it is shown that upon reduction a change of particle shape and distribution can occur. The size of the reduced particles can be estimated from the AFM images. The particle height and width as measured by AFM are about 3–4 and 30–50 nm, respectively, for the reduced sample. Due to the finite AFM tip diameter of 20 nm, the particle size probably appears larger. However, the measured values for the width still suggest that the particle width is larger than the height. Particle heights of at least 3–4 nm as measured by AFM are consistent with cluster sizes suggested by the peak position for the Rh in the XPS experiment.[37,21]

The ATR-FTIR spectra in Fig. 6 show that that adsorbed gas species can be observed. Since no peaks are distinguished for the sample without Rh, it is concluded that the CO is adsorbed to the Rh and that no interaction of the CO occurs with the ATR crystal. Furthermore, the thickness of the silica layer does not prevent the evanescent wave from probing the species adsorbed on the particles. In addition, any attenuation in the nanoparticles with a height of 4 nm does not significantly reduce the total transmittance through the crystal and a sensitivity of reflectance change of $\sim 5 \times 10^{-5}$ absorbance units can be reached.

The linearly bonded CO peak is observed at 2023 cm^{-1}. For RAIRS, peak positions between 1995 and 2074 cm^{-1} on Rh(100)[38] and between 1990 and 2070 cm^{-1} for Rh(111)[39] are reported, with increasing wave numbers for increasing coverage due to mutual interaction between the CO groups. Linearly adsorbed CO is observed with diffuse reflection infrared Fourier transform spectroscopy for highly dispersed Rh on silica at 2058–2065 cm^{-1} at room temperature, and at 2028 cm^{-1} at 498 K,[27] and for silica supported Rh at 2048–2067 cm^{-1}.[26,40] The fact that the peak of linear adsorbed CO in our case is observed at a lower frequency may indicate a low CO coverage or the formation of rhodium carbonyl hydride (H–Rh–CO), of which the CO stretch vibration is observed at 2020–2039 cm^{-1} for alumina supported Rh.[28,29] Although the hydrogen may originate from the hydroxylated surface or any residual H_2 from the reduction step, no change in OH content of hydroxylated SiOH groups around 3700–3500 cm^{-1} is observed upon CO exposure.

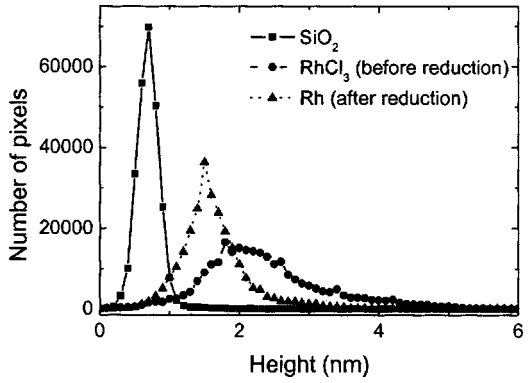

FIG. 5. Histogram of the AFM height values comparing the height distributions for a clean silica surface, and the Rh-covered samples before and after reduction.

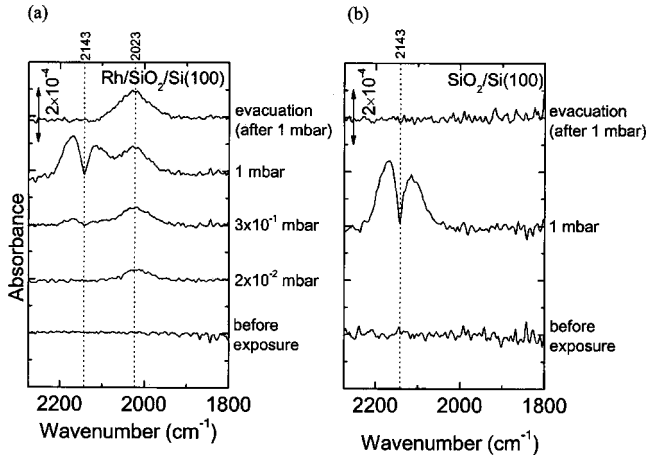

FIG. 6. Spectra of the exposure of CO to a silica/silicon ATR crystal with (a) and without (b) Rh nanoparticles before exposure, during dosing for different CO pressures, and after evacuation.

Apparently, all CO is linearly adsorbed. The signal to noise ratio was not sufficient to observe any bridged CO, expected around 1900 cm^{-1}.[26] Although bridged CO is often observed on Rh single crystals[38] and Rh polycrystalline electrodes,[41,42] a less intense bridged CO peak compared to the linearly adsorbed CO peak is also found for certain silica supported systems,[26,40,43,44] especially at CO pressures below 1 mbar.

The full width half maximum of the linearly adsorbed CO peak is 90 cm^{-1}. For single crystals, i.e., Rh(100), the width is on the order of 20–30 cm^{-1}.[38] The larger width in our case may be attributed to several reasons. The Rh nanoparticles consist of different surface types and include edge defects, although the (111) surface is the energetically most favorable. For example, for Pt nanoparticles, stabilized by dendrimers, large peak widths of $\sim$50 cm^{-1} are found for CO adsorption with liquid phase ATR infrared spectroscopy.[12] In addition, a distribution in the particle size may also cause a wider absorption peak. For example, for Au particles, a shift of 7 cm^{-1} to higher wave numbers for increasing particle size, corresponding to a coverage increase from 0.5 to 20 monolayers of Au, is reported for CO adsorption.[45] Moreover, 1 nm thick Pt films can exhibit dispersive, i.e., asymmetric and wide, band shapes for linearly adsorbed CO as measured with liquid phase ATR infrared spectroscopy.[11] In this reference, regular electromagnetic theory is used to explain this purely by the optical constants of the metal. Furthermore, the observed peak may consist of multiple peaks. Many report the presence of geminal dicarbonyls, i.e., $Rh^1(CO)_2$, resulting in two extra peaks at 2100 and 2030 cm^{-1},[26,40,43,44] besides the terminal CO peak at about 2060 cm^{-1}. In these references, these peaks did not shift in frequency when the exposure was changed, and therefore indicated that these Rh^1 sites were isolated on the oxide surface, formed by a reaction of the isolated Rh with both CO and OH of the support. For silica, this species was observed at pressures on the order of 100 mbar in combination with a negative peak around 3740 cm^{-1} belonging to isolated OH groups. In our case, the pressure is a factor of 100 lower and no clear negative peaks in that regions can be distinguished. However, experiments with other gases, e.g., ammonia, on this system also feature larger peak widths, which suggests an effect related to the particle or surface itself and not to the adsorbate.

Besides the linearly adsorbed CO peak, the P and R branches of gas phase CO are observed with a center frequency of at 2143 cm^{-1} for the Rh-covered sample with an integrated area of about 1.6×10^{-2} absorbance units $\times$ cm^{-1} for a CO pressure of 1 mbar in the front chamber and 3.5×10^{-3} mbar in the back chamber. This peak can in principle be either due to the evanescent wave probing the gas phase species close to the ATR crystal or to absorption in the direct beam path in the back chamber as some CO leaks into the back chamber. Which of these is the case was verified with the following calculation of the expected signal. The penetration depth of the evanescent wave into the vacuum is determined by the substrate and the vacuum and not by any intermediate thin layer[20,22] and is about 0.4 μm for a wave number of 2000 cm^{-1}. This is much smaller than the infrared internal beam path length in the back side of the chamber, which is about 50 cm. For absorption in the direct beam path, and a CO absorption cross section σ for gas phase CO at 2143 cm^{-1} of 1.036×10^{-17} $cm^2\times cm^{-1}$/molecule[46] assuming a linear dependence, the measured peak area corresponds to a calculated pressure of 3×10^{-3} mbar which is in agreement with the measured CO pressure in the back chamber. For the sample without Rh, this peak is 30% higher than for the one with Rh, which is related to a different pressure in the back chamber due to a different leakage rate for each individual sample. Therefore, the gas phase peak is due to residual gas phase CO in the back side of the chamber.

An exact quantitative description of the relation between the peak area of the linearly adsorbed CO and the CO surface coverage in our system is difficult, not only because randomly distributed particles are considered, but also because of both attenuation in the metallic particles and possible electric field enhancement on the surface.[24,25] However, an estimate can be made if the formation of a monolayer of CO on a flat surface with a Lorentz oscillator model is

assumed[8,20,22,47] and if we ignore any light coherence and light scattering effects. An expression for the absorbance as a function of coverage can be found in the Appendix for *S*- and *P*-polarized light. The geometric average is taken to obtain the absorbance for nonpolarized light. With this expression, the peak area of the linearly adsorbed CO in Fig. 6(a), which is 9×10^{-3} absorbance units$\times$cm^{-1}, yields a coverage of about $\sim$0.04 CO per nm^2. Considering the effect of the thin silica layer on the evanescent wave, the absorbance is reduced to 80% as mentioned in Sec. I, resulting in a surface coverage of $\sim$0.05 CO per nm^2. The minimum detectable coverage is about a factor of 10 lower, corresponding to $\sim$0.005 CO per nm^2 substrate area or about 5×10^{-4} monolayers, taking 1 monolayer as $\sim$10 CO molecules per nm^2. As a reference, typical sensitivities of $\sim10^{-3}$ CO monolayers have been achieved for RAIRS.[39]

The CO coverage is obviously related to the available surface area of the nanoparticles, which can be roughly estimated by analysis of the AFM data. When using the rough assumption, for simplicity, that the Rh particles are spherical with a diameter of 4 nm, this corresponds to a particle surface area of about 50 nm^2. Rhodium has a face-centered cubic lattice with a lattice constant of 0.380 nm. This gives a number of Rh atoms per unit surface area of 14 Rh/nm^2, which results in $\sim$700 atoms on the outside surface of each particle. The Rh particle density is about 200 per μm^2, which then corresponds to an estimated $\sim$0.14 available adsorption sites per nm^2 substrate area. With the coverage of $\sim$0.05 CO per nm^2 substrate area, estimated from data using the Lorentz oscillator model, this then results in a measured coverage of about $\sim$0.36 CO per Rh. For exposures of Rh single crystals to CO, 1 mbar easily leads to the saturation coverage of about 0.75 ML for both Rh(100)[38] and Rh(111),[48] so it is expected that the actual coverage in our case is higher than this value of $\sim$0.36 CO per Rh. However, this is still a good agreement, when taking all aforementioned approximations concerning the Rh particles into account. In addition, the measured coverage may not be at its maximum, as suggested earlier. Moreover, because of the infrared attenuation in the Rh particles, the detection is less sensitive to CO adsorbed on top of the particles than to CO on the sides of the particles while any electric field enhancement may increase the sensitivity. For flat particles, as suggested by AFM, more CO is adsorbed on top of the particles than on the sides. In addition, it is noted that not only the size but also the density and distribution of Rh particles determine the total transmittance of the IR light that is measured in the detector. Beam paths with many reflections on the relatively few randomly distributed Rh-covered sites per beam path have a lower total transmittance compared to beam paths with fewer reflections on these sites. The former beam paths probably probe more CO molecules while the latter contribute most to the total transmittance. As a result, the exact overall sensitivity loss due to attenuation in the Rh particles is hard to calculate. Nevertheless, the available Rh surface area as determined by AFM and the amount of CO per substrate area as measured by ATR-FTIR result in a CO coverage per Rh atom comparable in magnitude to the expected saturation coverage.

V. CONCLUSIONS

It is shown that attenuated total reflection Fourier transform infrared spectroscopy (ATR-FTIR) can be applied to the detection of adsorbed gaseous species on planar model catalysts, which consist of metallic (Rh) nanoparticles supported by a silicon ATR crystal with a thin hydroxylated silica layer. In the ATR-FTIR spectrum, the noise level is $\sim5\times10^{-5}$ absorbance units in the region of 4000–1500 cm^{-1}. When the ATR crystal with Rh nanoparticles is exposed to CO, a stretch vibration peak is observed at 2023 cm^{-1} due to linearly adsorbed CO on Rh. The peak width is 90 cm^{-1}, which suggests the presence of different surface types and edge defects. Assuming a Lorentz oscillator model, the integrated peak area is translated into a coverage of $\sim$0.05 CO per nm^2 substrate area. With an estimation of the available Rh surface area obtained by AFM analysis, this results in a coverage of $\sim$0.36 CO per Rh atom, which is in fair agreement with the expected saturation coverage for Rh single crystals of about 0.75 ML. No bridged CO or geminal dicarbonyls are observed for exposures up to 1 mbar. For CO, a sensitivity of $\sim5\times10^{-4}$ monolayers can be achieved for 3000 scans, which is valid for various types of surfaces, and which is an improvement over the typical sensitivity of RAIRS, i.e., $\sim1\times10^{-3}$ CO monolayers. The ATR-FTIR approach to measure vibrational spectra described here substantially expands the opportunities for investigating adsorbates on planar model catalysts.

ACKNOWLEDGMENTS

Dr. J. P. M. Hoefnagels is acknowledged for the design of the ATR-FTIR and vacuum setup. Han Wei is acknowledged for his assistance with the silica hydroxylation while M. J. F. van de Sande and J.F.C. Jansen are acknowledged for their technical assistance. The research of Dr. W. M .M. Kessels was made possible by a fellowship of the Royal Netherlands Academy of Arts and Sciences (KNAW). This work was supported by the Netherlands Foundation for Fundamental Research on Matter (FOM).

APPENDIX

For an absorption measurement in transmission, the absorbance A is given by $A\approx\alpha d/\ln 10$, where αd is the absorption coefficient times the film thickness with $\alpha=4\pi nk\tilde{\nu}$ with $\tilde{\nu}$ the wave number and $2nk=\varepsilon_2$, the imaginary part of the dielectric function ε. So, the absorbance is a function of d and ε_2.

For internal reflection at a surface of an ATR crystal covered with adsorbates, the relation between the absorbance and the surface coverage of the adsorbates can be derived with a three-layer model, i.e., substrate, adsorbates, and the

low index medium, i.e., vacuum in our case.[8,20] For a single reflection, the absorbances for S and P polarization are given by

$$A_S = \frac{2\pi\tilde{\nu}\varepsilon_2 d}{\ln 10\sqrt{\varepsilon_s}\cos\theta}E_y^2$$

$$A_P = \frac{2\pi\tilde{\nu}\varepsilon_2 d}{\ln 10\sqrt{\varepsilon_s}\cos\theta}\left(E_x^2 + \frac{\varepsilon_v^2}{|\varepsilon|^2}E_z^2\right). \tag{A1}$$

Here, ε_s is the dielectric function of the substrate ($\varepsilon_s = n_s^2 = 11.7$ for silicon), and $\varepsilon_\nu = 1$ that of the low index medium, and ε represents the dielectric function of the adsorbates. $\tilde{\nu}$ is the wave number of the incoming light, d the effective layer thickness, and θ the angle of incidence with respect to the surface normal. E_x, E_y, and E_z, are the dimensionless electric field intensities, i.e., normalized to the incoming field. Their intensities are given by

$$E_y^2 = \frac{4\cos^2\theta}{\left(1-\frac{\varepsilon_v}{\varepsilon_s}\right)},$$

$$E_x^2 = \frac{4\cos^2\theta}{\left(1-\frac{\varepsilon_v}{\varepsilon_s}\right)}\frac{\sin^2\theta - \frac{\varepsilon_v}{\varepsilon_s}}{\left(1+\frac{\varepsilon_v}{\varepsilon_s}\right)\sin^2\theta - \frac{\varepsilon_v}{\varepsilon_s}}, \tag{A2}$$

$$E_z^2 = \frac{4\cos^2\theta}{\left(1-\frac{\varepsilon_v}{\varepsilon_s}\right)}\frac{\sin^2\theta}{\left(1+\frac{\varepsilon_v}{\varepsilon_s}\right)\sin^2\theta - \frac{\varepsilon_v}{\varepsilon_s}}.$$

It should be noted that the electric fields, as given by the above expressions, and hence the absorbances decrease when the thickness is large compared to the wavelength or the attenuation if the layer is high, i.e., $2\pi d/\lambda_1 > 0.1$ or $k_2 > 0.1$.[20] Here, k_2 is the attenuation coefficient. In the case of a monolayer of adsorbates instead of a (macroscopic) thin film, the values of d and $\varepsilon(=\varepsilon_1 + i\varepsilon_2)$ should be redefined and can be expressed as[8]

$$d = \frac{4\pi S}{U_0}$$

and

$$\varepsilon(v) = 1 + U_0\alpha_e + \frac{\tilde{\nu}_0^2}{\tilde{\nu}_0^2 - \tilde{\nu}^2 - i\Gamma\tilde{\nu}}U_0\alpha_v(0). \tag{A3}$$

Here, S is the surface density (number per unit area) of the oscillators, α_e is the vibrational polarizability of the adsorbed molecule, $\alpha_\nu(0)$ the electronic polarizability, U_0 the summation term of the dipole distances, a measure for the arrangements of the dipoles,[8] $\tilde{\nu}_0$ the wave number of the absorption, and Γ the peak width. For multiple reflections, the expressions for the integrated absorbances for S and P polarization are given below, which are derived by combining Eqs. (A1)–(A3) and carrying out the integration with help from formulas from Ref. 8

$$\int A d\tilde{\nu}\Big|_S = \frac{4\pi^2}{\ln 10}N\tilde{\nu}_0^2\alpha_v(0)S\frac{4\pi\cos\theta}{\sqrt{\varepsilon_s}\left(1-\frac{\varepsilon_v}{\varepsilon_s}\right)},$$

$$\int A d\tilde{\nu}\Big|_P = \frac{4\pi^2}{\ln 10}N\tilde{\nu}_0^2\alpha_v(0)S\frac{4\pi\cos\theta}{\sqrt{\varepsilon_s}\left(1-\frac{\varepsilon_v}{\varepsilon_s}\right)} \times \frac{\left(1+\frac{\varepsilon_v^2}{\varepsilon_\infty^2}\right)\sin^2\theta - \frac{\varepsilon_v}{\varepsilon_s}}{\left(1+\frac{\varepsilon_v}{\varepsilon_s}\right)\sin^2\theta - \frac{\varepsilon_v}{\varepsilon_s}} \tag{A4}$$

with $\varepsilon_\infty = 1 + U_0\alpha_e$. Here, N is the number of internal reflections on the crystal side to be studied, i.e., $N=25$ in our case. For CO on Rh(100), values of α_e, $\alpha_\nu(0)$, and U_0 are 1.8 Å^3, 0.48 Å^3, and 0.3 Å^{-3}, respectively, and can be used as a first approximation[38] for our situation of CO adsorbed on Rh particles. In addition, $\tilde{\nu}_0$ is about 2000 cm^{-1} for the stretch vibration of linearly bound CO. And, as mentioned before, $\theta = 45°$, $\varepsilon_s = 11.7$, and $\varepsilon_\nu = 1$ for our system. In this way, a direct relation is obtained between the absorbance A and the number of COs per unit area S.

[1] P. L. J. Gunter, J. W. Niemantsverdriet, F. H. Ribeiro, and G. A. Somorjai, Catal. Rev. - Sci. Eng. **39**, 77 (1997).
[2] C. R. Henry, Surf. Sci. Rep. **31**, 231 (1998).
[3] D. R. Rainer and D. W. Goodman, J. Mol. Catal. A: Chem. **131**, 259 (1998).
[4] H.-J. Freund, M. Baumer, and H. Kuhlenbeck, Adv. Catal. **45**, 333 (2000).
[5] A. Borgna, E. J. M. Hensen, J. A. R. van Veen, and J. W. Niemantsverdriet, J. Catal. **221**, 541 (2004).
[6] D. W. Goodman, J. Vac. Sci. Technol. A **14**, 1526 (1996).
[7] H. Unterhalt, G. Rupprechter, and H.-J. Freund, J. Phys. Chem. B **106**, 356 (2002).
[8] Y. J. Chabal, Surf. Sci. Rep. **8**, 211 (1988).
[9] S. F. Bent, M. L. Schilling, W. L. Wilson, H. E. Katz, and A. L. Harris, Chem. Mater. **6**, 122 (1994).
[10] M. Burgener, R. Wirz, T. Mallat, and A. Baiker, J. Catal. **228**, 152 (2004).
[11] T. Bürgi, Phys. Chem. Chem. Phys. **3**, 2124 (2001).
[12] D. Liu, J. Gao, C. J. Murphy, and C. T. Williams, J. Phys. Chem. B **108**, 12911 (2004).
[13] C. Kerresszegi, D. Ferri, T. Mallatt, and A. Baiker, J. Phys. Chem. B **109**, 958 (2005).
[14] V. M. Bermudez, J. Electrochem. Soc. **152**, F31 (2005).
[15] P. Rigler, W.-P. Ulrich, P. Hoffmann, M. Mayer, and H. Vogel, ChemPhysChem **4**, 268 (2003).
[16] Y. J. Chabal, G. S. Higashi, and S. B. Christman, Phys. Rev. B **28**, 4472 (1983).
[17] D. C. Marra, E. A. Edelberg, R. L. Naone, and E. S. Aydil, J. Vac. Sci. Technol. A **16**, 3199 (1998).
[18] W. M. M. Kessels, D. C. Marra, M. C. M. van de Sanden, and E. S. Aydil, J. Vac. Sci. Technol. A **20**, 781 (2002).
[19] S. Bocharov and A. V. Teplyakov, J. Am. Chem. Soc. **125**, 7196 (2003).
[20] N. J. Harrick and F. K. du Pré, Appl. Opt. **5**, 1739 (1966).
[21] J. W. Niemantsverdriet, A. F. P. Engelen, A. M. de Jong, W. Wieldraaijer, and G. J. Kramer, Appl. Surf. Sci. **144–145**, 366 (1999).
[22] N. J. Harrick, J. Opt. Soc. Am. **55**, 851 (1965).
[23] N. J. Harrick, *Internal Reflection Spectroscopy*, (Wiley New York, 1967).
[24] M. Osawa, K. I. Ataka, K. Yoshii, and Y. Nishikawa, Appl. Spectrosc. **47**, 1497 (1993).
[25] D. Ferri, T. Bürgi, and A. Baiker, J. Phys. Chem. B **105**, 3187 (2001).
[26] P. Basu, D. Panayotov, and J. T. Yates, Jr., J. Phys. Chem. **91**, 3133

(1987).
[27]S. Trautmann and M. Baerns, J. Catal. **150**, 335 (1994).
[28]F. Solymosi, A. Erdöhelyi, and M. Kocsis, J. Catal. **65**, 428 (1980).
[29]F. Solymosi, A. Erdöhelyi, and M. Kocsis, J. Catal. **70**, 451 (1981).
[30]J. A. Anderson and C. H. Rochester, J. Chem. Soc., Faraday Trans. **86**, 3809 (1990).
[31]K. Ashley, A. Sehgal, E. J. Amis, D. Raghavan, and A. Karim, Mater. Res. Soc. Symp. Proc. **700**, S4.7.1 (2002).
[32]*Handbook of X-ray Photoelectron Spectroscopy*, edited by J. F. Moulder, W. F. Stickle, P. E. Sobol, K. D. Bomben, and J. Chastain (Perkin-Elmer Company, Eden Prairie, MN, 1992).
[33]J. P. M. Hoefnagels, E. Langereis, W. M. M. Kessels, and M. C. M. van de Sanden, IEEE Trans. Plasma Sci. **33**, 234 (2005).
[34]R. P. Sperline, Appl. Spectrosc. **45**, 677 (1991).
[35]H. J. Borg, L. C. van den Oetelaar, L. J. van IJzendoorn, and J. W. Niemantsverdriet, J. Vac. Sci. Technol. A **10**, 2737 (1992).
[36]H. J. Borg, L. C. van den Oetelaar, and J. W. Niemantsverdriet, Catal. Lett. **17**, 81 (1993).
[37]M. G. Mason, Phys. Rev. B **27**, 748 (1983).
[38]A. M. de Jong and J. W. Niemantsverdriet, J. Chem. Phys. **101**, 10126 (1994).
[39]F. M. Hoffmann, Surf. Sci. Rep. **3**, 107 (1983).
[40]P. Basu, D. Panayotov, and J. T. Yates, Jr., J. Am. Chem. Soc. **110**, 2074 (1988).
[41]G.-Q. Lu, S.-G. Sun, L.-R. Cai, S.-P. Chen, Z.-W. Tian, and K.-K. Shiu, Langmuir **16**, 778 (2000).
[42]E. Ivanova and K. Hadjiivanov, Phys. Chem. Chem. Phys. **5**, 655 (2003).
[43]S. Bernal, G. Blanco, J. J. Calvino, M. A. Cauqui, J. M. Rodríguez-Izquierdo, and H. Vidal, J. Alloys Compd. **250**, 461 (1997).
[44]J. T. Yates, Jr. and K. Kolasinki, J. Chem. Phys. **79**, 1026 (1983).
[45]D. R. Rainer, C. Xu, P. M. Holmblad, and D. W. Goodman, J. Vac. Sci. Technol. A **15**, 1653 (1997).
[46]L. S. Rothman *et al.*, J. Quant. Spectrosc. Radiat. Transf. **48**, 469 (1991).
[47]J. D. E. McIntyre and D. E. Aspnes, Surf. Sci. **24**, 417 (1971).
[48]K. A. Peterlinz, T. J. Curtiss, and S. J. Sibener, J. Chem. Phys. **95**, 6972 (1991).